Article

Adaptive Spatiotemporal SVD Clutter Filtering for Ultrafast Doppler Imaging Using Similarity of Spatial Singular Vectors

BARANGER, Jerome, *et al*.

Abstract

Singular value decomposition of ultrafast imaging ultrasonic data sets has recently been shown to build a vector basis far more adapted to the discrimination of tissue and blood flow than the classical Fourier basis, improving by large factor clutter filtering and blood flow estimation. However, the question of optimally estimating the boundary between the tissue subspace and the blood flow subspace remained unanswered. Here, we introduce an efficient estimator for automatic thresholding of subspaces and compare it to an exhaustive list of thirteen estimators that could achieve this task based on the main characteristics of the singular components, namely the singular values, the temporal singular vectors, and the spatial singular vectors. The performance of those fourteen estimators was tested in vitro in a large set of controlled experimental conditions with different tissue motion and flow speeds on a phantom. The estimator based on the degree of resemblance of spatial singular vectors outperformed all others. Apart from solving the thresholding problem, the additional benefit with this estimator was its denoising [...]

Reference

UNIVERSITÉ
DE GENÈVE

Adaptive Spatiotemporal SVD Clutter Filtering for Ultrafast Doppler Imaging Using Similarity of Spatial Singular Vectors

Jérôme Baranger, Bastien Arnal, Fabienne Perren, Olivier Baud, Mickael Tanter, and Charlie Demené

Abstract—Singular value decomposition of ultrafast imaging ultrasonic data sets has recently been shown to build a vector basis far more adapted to the discrimination of tissue and blood flow than the classical Fourier basis, improving by large factor clutter filtering and blood flow estimation. However, the question of optimally estimating the boundary between the tissue subspace and the blood flow subspace remained unanswered. Here, we introduce an efficient estimator for automatic thresholding of subspaces and compare it to an exhaustive list of thirteen estimators that could achieve this task based on the main characteristics of the singular components, namely the singular values, the temporal singular vectors, and the spatial singular vectors. The performance of those fourteen estimators was tested *in vitro* in a large set of controlled experimental conditions with different tissue motion and flow speeds on a phantom. The estimator based on the degree of resemblance of spatial singular vectors outperformed all others. Apart from solving the thresholding problem, the additional benefit with this estimator was its denoising capabilities, strongly increasing the contrast to noise ratio and lowering the noise floor by at least 5 dB. This confirms that, contrary to conventional clutter filtering techniques that are almost exclusively based on temporal characteristics, efficient clutter filtering of ultrafast Doppler imaging cannot overlook space. Finally, this estimator was applied *in vivo* on various organs (human brain, kidney, carotid, and thyroid) and showed efficient clutter filtering and noise suppression, improving largely the dynamic range of the obtained ultrafast power Doppler images.

J. Baranger, B. Arnal, M. Tanter, and C. Demené are with the Institut Langevin, ESPCI ParisTech, Paris Sciences et Lettres Research University, CNRS UMR7587, INSERM U979, 75006 Paris, France (e-mail: jerome.baranger@espci.fr; bastien.arnal@espci.fr; mickael.tanter@espci.fr; charlie.demene@espci.fr).

F. Perren is with the Neurology Department, Neurosonology Unit, Geneva University Hospital, 1205 Geneva, Switzerland (e-mail: fabienne.perren@hcuge.ch).

O. Baud is with the Assistance Publique - Hôpitaux de Paris, Neonatal Intensive Care Unit, Inserm U1141, Fondation PremUp, Robert Debré University Hospital, 75019 Paris, France (e-mail: olivier.baud@aphp.fr).

Index Terms—Blood flow, Doppler imaging, ultrafast imaging, ultrasound, singular value decomposition

I. Introduction

ULTRAFAST ultrasound imaging introduced a new paradigm for Doppler imaging [1]. By using unfocused wave transmissions, it enables the acquisition of a large number of synchronous ultrasonic samples at a very high framerate in all the field of view. The primary effect is the substantial increase in sensitivity to blood flow in Doppler imaging after clutter filtering, by a factor up to 30 [2]. This increased sensitivity lead to numerous clinical application, for example in cardiac imaging [3] or liver vascular imaging [4], but also opened a whole new playground in fundamental research with functional imaging [5]–[7] and preclinical applications [8], [9]. In all these examples, clutter filtering, which discriminates between blood flow and tissue signal, is critical: when targeting quantitative measurements, tissue motion can be a major source of artefacts and corrupt the measured level of blood volume or blood flow. The large number of synchronous samples available with Ultrafast ultrasound imaging does not only improve the sensitivity to blood flow, it also enables a more efficient discrimination of the tissue signal. Usually the clutter is removed using a high pass filter [10], but this strategy only takes into account the low frequency nature of the tissue motion. Tissue motion is also spatially coherent in that when the tissue in one location moves, the tissue in the surrounding area tend to move the same way because of its cohesive nature. On the other hand blood motion does not exhibit this spatial coherence due to the constant rearrangement of the blood scatterers. Ledoux *et al* [11] proposed a clutter reduction based on the Singular Value Decomposition of the correlation matrix between successive temporal samples of a M-mode line in a simulation study. In this approach 1D information between adjacent lines was used via the diagonalization of the spatiotemporal (time and depth) correlation matrix. Several methods based on this concept were proposed following this work. Yu and Lovstakken [12] in 2010 propose an exhaustive review of these methods Among those developments, important works such as the down-mixing approach using an eigen-based tissue motion estimation of Bjaerum *et al* [13] and the real time implementation of eigen-based clutter rejection proposed by Lovstakken *et al* [14] have to be cited.

Kruse and Ferrara [15] also developed an original high frequency swept scan imaging setup whose datasets were processed using principal component analysis to estimate blood velocity in presence of strong motion. In a previous paper (Demene *et al*. 2015), we proposed a clutter filter particularly adapted to ultrafast imaging data. We used both temporal and spatial information to remove clutter in the framework of Ultrafast ultrasound imaging, by computing the singular value decomposition of the space-time matrix (two dimensions for space and one dimension for time) of the ultrasonic data. This decomposition turns the matrix into a weighted, ordered sum of separable matrices, separable meaning written as the outer product of a spatial and a temporal vector. Tissue signal and blood signal having different spatiotemporal statistics, clutter filtering is performed by recombining only the separable matrix associated to the smallest singular values and containing blood flow information. This hard thresholding rule (i.e. replacing the whole subset of the biggest singular values by zeros) was chosen under the assumption that tissue and blood signals are described by orthogonal singular vectors subspaces, but Candès *et al* [16] and [17], and Otazo *et al*. [18] also introduced a soft-thresholding strategies for MRI clutter filtering by weighting each singular values. We showed that SVD-based spatiotemporal filtering was much more efficient to remove clutter than a classical high-pass filter or a down-mixing filter, especially in the case of very slow blood flows or strong motion artifacts. This increase in efficiency is due to the large number of samples and their synchronicity in space proper to Ultrafast imaging, and this explains why previous attempts to use SVD to filter focused ultrasonic data did not show very significant improvement [12], [15]. As compared to conventional FIR or IIR filters, SVD filter has two important differences. Firstly, SVD does not suffer from the well-known initialization issue. And secondly, where IIR/FIR filters use the Fourier basis to represents the data, SVD generates a new basis specific to the data.

However, there is still no standardized approach to the problem of choosing the rank of the singular value marking the boundary between the tissue and the blood flow subspaces. This issue is crucial since the optimal threshold varies dramatically with the imaging conditions: it will increase with the velocities of tissue and also depends on the velocities of blood flows. Fig. 1 depicts the classical example of strong motion artefacts when the threshold is taken too low: the two images have been acquired in the same imaging plane with a few seconds interval: in the first row no motion was present and a low threshold of 60 rejected singular values is enough for complete tissue removal; but in the second row, tissue motion was present and a fixed threshold at 60 singular values results in a strong flashing artefact. At least 100 singular values had to be rejected for complete tissue removal.

In the present paper we present an extensive performance evaluation of several proposed estimators for the choice of this singular value threshold, taking advantage of all the SVD features: energetic information provided by the singular values, temporal behavior given by the right singular vectors, or spatial distribution encoded in left singular vectors. We assessed their efficiency *in vitro* for a wide range of tissue speeds (in plan
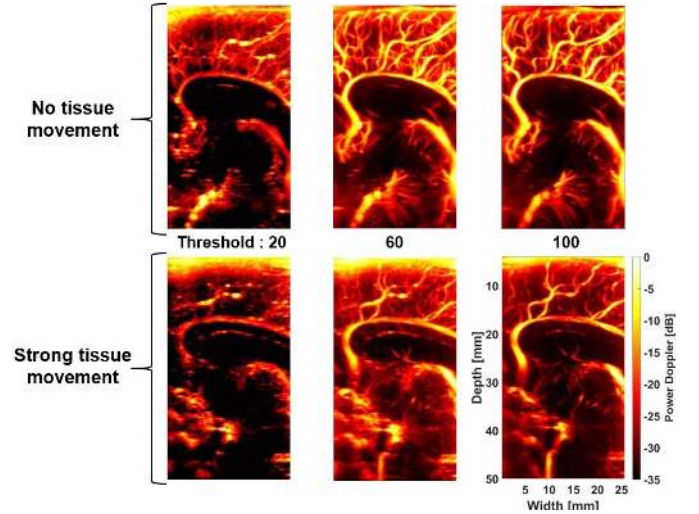

Fig. 1. Optimal SVD threshold changes with tissue movement. Two Ultrafast Doppler acquisitions on neonate brain performed in a sagittal plane. The patient was still during the first acquisition (top row), but moved during the second acquisition (bottom row).

and out-of-plane) and flow speeds, in order to determine the best estimator, and finally the latter is confronted to real-life *in vivo* clutter filtering situations. This thorough comparison enables us to identify one approach outperforming the other thresholding methods, which could be envisioned as a good candidate for future standardization.

II. THEORY

The ultrasonic data are represented under the form of a variable $s(x, z, t)$ of size (n_z, n_x, n_t). Its sampling is rearranged into a 2D space-time Casorati matrix S of dimension $(n_x \times n_z, n_t)$ [16]. Then, the singular value decomposition of this matrix S is written as:

$$S = U\Delta V^*$$ (1)

Where Δ is a non-square $(n_x \times n_z, n_t)$ diagonal matrix with diagonal coefficients λ_k, matrices U and V are orthonormal matrices of rank n_t with respective dimensions $(n_x \times n_z, n_x \times n_z)$ and (n_t, n_t), and $*$ stands for the conjugate transpose. Columns of U and V matrices correspond respectively to the spatial (left) and temporal (right) singular vectors of S. This decomposition can be made so that the coefficients in the diagonal matrix Δ are sorted in a descending order. In that case tissue signal, with higher energy and higher spatial coherence, will be concentrated on the first singular vectors. Thus, a suppression of the tissue signal can be achieved by using a "brick-wall" filtering matrix I^f that removes the contribution of the first singular values from the original signal. This gives the filtered signal S^f:

$$S^f = U\Delta I^f V^*$$ (2)

This matrix I^f is diagonal and the first N diagonal coefficients are zeros whereas the remaining diagonal coefficients are ones. This formalism and filtering has been described in details in a previous article [19], but the question of how to optimally
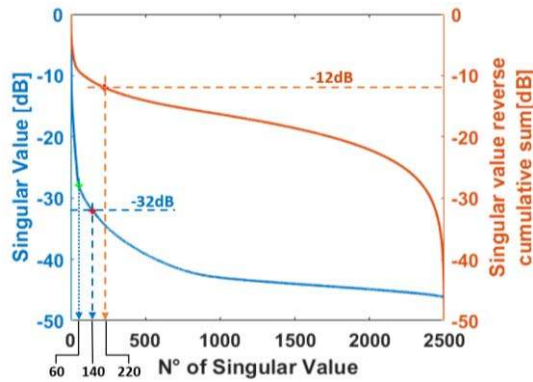
Fig. 2. Energetic criteria for threshold selection. Singular values of the matrix Δ (solid blue) and blood subspace energy (solid orange) computed as the reverse cumulative sum of singular values. Acquisition on the brain of a neonate. A first natural threshold can be obtained by arbitrarily defining a magnitude above which the singular values are considered to represent tissue signal (dashed blue). Here, a magnitude chosen at -32dB would result in a threshold at 140. Same approach can be done for the blood energy curve: a cutoff chosen at -12dB (dashed orange) gives a threshold of 220. Another threshold is the turning point of the singular value curve (dotted blue), which here gives a threshold of 60.

choose N was left open. This is the principal matter of this paper, and we wanted to be exhaustive. The SVD thresholding can be performed using four different kinds of methods listed below.

A. Arbitrary Threshold

The basic intuitive approach is to manually tune the threshold N for a given acquisition, until the resulting Power Doppler image is acceptable. One can think of first performing this manual estimation for several examples in a particular clinical setup, giving rise to a lookup table with preset thresholds for a range of particular experimental conditions (breast, thyroid, brain, etc.). This arbitrary threshold relies on qualitative criteria and assume that the clutter is comparable from one acquisition to another as long as imaging conditions are similar. Being parametric and independent of the real ultrasonic signal characteristics, the arbitrary threshold may exhibit a lack of robustness. In the following, we propose some more complex estimators.

B. Estimators Based on the Singular Values

The distribution of the singular values can give several ideas to estimate the rejection threshold N. As the singular vectors are normalized ($\forall i\, U_i^* \cdot U_i = 1$ and $\forall i\, V_i \cdot V_i^* = 1$), the amount of energy in a particular couple of singular vectors is entirely contained in the singular value λ_i.

A first idea is to decide that singular values above a certain threshold in dB (compared to the sum of all singular values) are rejected (Fig. 2, blue dashed line). This can be thought as an improvement on the arbitrary threshold: in certain conditions of tissue motion and blood flow speed the best threshold is found and the corresponding dB level is calculated. This dB level is then used to estimate the threshold in another set of tissue motion and blood flow speed. However this do not
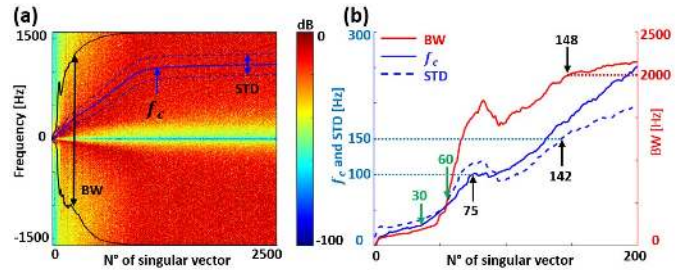

Fig. 3. Temporal criteria for threshold selection. (a) Power spectral density of temporal singular vectors. Acquisition on the brain of a neonate. (b) f_c, STD and BW are shown on smaller singular vector range (0 to 200). Each dotted line stands for a cutoff value used to define a singular vector threshold on the associated curve (black arrows). Green arrows show the first inflexion points of the curves (30 for f_c, 60 for STD and BW).

take into account that tissue and blood flow are decomposed on two multidimensional subspaces, and as such that it is more relevant to consider the energy associated with a space spanning over a subspace of singular vector, i.e. the sum of the associated singular values.

Therefore a second idea is to think the overall signal as an additive combination of a tissue signal and a blood signal. As such, given an ultrasound emission frequency, a characterized transducer and standard echogenicity conditions in a certain organ, the tissue signal and blood signal have a given backscattered energy. It can then be decided to choose the threshold when the ratio between the cumulative sum of the blood singular values and the overall signal energy, defined as the sum of all singular values (Eq. 3), reaches a certain (negative) dB level (Fig. 2, orange dashed line).

$$\frac{Blood\ energy}{Total\ energy} = \frac{\sum_{k=N}^{Rank(S)} \lambda_k}{\sum_{k=1}^{Rank(S)} \lambda_k} \quad (3)$$

The last idea is a non-parametric one. The blood flow signal can be thought as an intermediate between the highly coherent tissue signal and the Gaussian image noise, the singular values of the latter following a Marchenko-Pastur distribution [20]. This assertion is supported by the experience, showing that singular value decomposition of *in vivo* ultrafast imaging data usually exhibits 3 different regimes of singular value decrease (Fig. 2, blue curve). The first regime is supposed to be related to tissue components and the clutter rejecting threshold is chosen as the first turning point of the singular value curve (blue dotted line), given by the first local minimum of the curvature radius.

C. Estimators Based on the Temporal Singular Vectors **V**

Looking for particular characteristics of the temporal vectors **V** easily comes to mind in the ultrasound community, because clutter filtering is usually done with a high pass filter rejecting signal below a certain frequency (i.e. a certain speed). Thus tissue and blood flow are generally assumed to exhibit distinct frequency content. One can therefore expect the temporal vectors to follow the same trend.

Fig. 3(a) shows the power spectral density (PSD) of all temporal vectors for an acquisition on a neonate's brain. It is

noticeable that the spectra are almost equally spread between positive and negative frequencies. It implies that most spectral statistics such as the central frequency have to be computed side-by-side of the band. For each temporal singular vector, the PSD-weighted central frequency (f_c, first statistical moment) and standard deviation (STD, second statistical moment) of the considered half band were computed. As expected, the central frequency and the STD increases with the singular vector index.

Another interesting statistics is that tissue signal generally has a narrower bandwidth than blood flow signal. This property is directly linked to the blood higher decorrelation rate [21], and is the base of Bandwidth imaging [22]. This behavior is shown by the evolution of the bandwidth containing 99% of the energy (Fig. 3 a), which is computed over the whole frequency band (two-sided).

For each of these 3 spectral statistics, we can define 2 SVD threshold estimators. Firstly, we could consider singular vectors to be in the tissue subspace while their central frequency, frequency STD or 99% bandwidth (BW) lies below a given cutoff. For instance (Fig. 3 b), singular vectors whose central frequency are below 100Hz are thought to be tissue representatives, which boils down to a tissue/blood threshold of $N = 75$. Secondly, non-parametric estimators can be defined by the first inflexion point of these curves (Fig. 3 b, green arrows), following the idea that these spectral statistics experience a change of regime around the transition between tissue and blood subspaces.

D. Estimators Based on the Spatial Singular Vectors **U**

So far, we considered the energetic and temporal information provided respectively by the singular values in Δ and the temporal singular vectors in V. But the spatial features U of the SVD decomposition also hold interesting statistics. Thus, in a previous paper [23], we introduced an automated SVD-based filter that was able to adaptively determine the singular vectors subspace describing the signal from cavitation bubbles. A close approach is used here for blood subspace determination and relies on the following concepts. From Eq. 1 we can write S as the sum of multiple separable matrices $u_k v_k^*$, of size $(n_x \times n_z, n_t)$, weighted by the singular value λ_k where u_k and v_k are respectively the k-th column vector of U and V (Eq. 4).

$$S = \sum_{k=1}^{n_t} \lambda_k \cdot u_k v_k^* \qquad (4)$$

Each vector u_k has a size $(n_x \times n_z, 1)$ and then could be rearranged in the shape of a 2D image of size (n_z, n_x). Therefore, each matrix $u_k v_k^*$ can be thought as an image of intensity $|u_k|$, with a pixel-specific phase shift $arg(u_k)$, and modulated along time by a complex signal v_k (the symbols modulus $||$ and argument $arg()$ being applied to each components of u_k). If we consider that the tissue signal and the blood signal have different spatial distributions, then the $|u_k|$ vectors should be correlated within the tissue subspace and within the blood subspace, but not between them. This assumption on the spatial distribution is widely observed experimentally, with the tissue being spread in the whole field of view, with
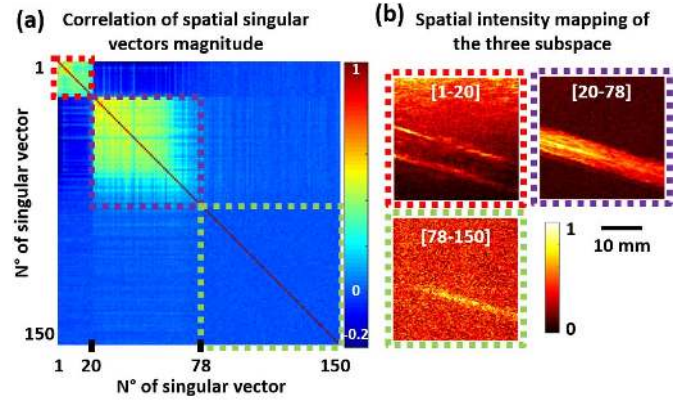

Fig. 4. Spatial criteria for threshold selection. (a) Incoherent correlation matrix of spatial singular vectors, for a plane wave ultrafast Doppler acquisition on a flux phantom. Three highly correlated areas appear. (b) Spatial vectors are incoherently averaged in the 3 areas, giving intensity maps. From 1 to 20 (red dotted squares), vectors describe the tissue and the canal walls. From 20 to 78 (purple dotted squares), spatial vectors represent the blood flow. From 78 to 150, spatial vectors account for mostly noise, yet with remaining blood signal.

high spatial and temporal coherence, and the blood being restricted to the vascular network, with lower spatial and temporal coherence. Consequently, $\mathbf{C}$, the correlation matrix of $|u_k|_{k \in [[1, n_t]]}$ of size (n_t, n_t) should reveal the different subspaces. Its calculation is given in Eq. 5, where $\overline{u}_n$ and σ_n respectively stand for the mean and the standard deviation of u_n indexes.

$$C(n, m) = \frac{1}{n_x \cdot n_z}$$
$$\cdot \sum_{p}^{n_x \cdot n_z} \frac{(|u_n(p)| - \overline{|u_n|}) \cdot (|u_m(p)| - \overline{|u_m|})}{\sigma_n \cdot \sigma_m},$$
$$(m, n) \in [[1, n_t]]^2 \qquad (5)$$

We will now refer to that correlation matrix $\mathbf{C}$ as the spatial similarity matrix, which is shown in Fig. 4(a) in the *in vitro* case of a tissue phantom with an embedded canal filled with blood mimic fluid and later in Fig. 10(a) in the *in vivo* case of a neonate brain acquisition. In the almost ideal circumstances of the phantom where tissue and blood areas almost do not overlap, tissue and blood subspaces are revealed by clearly identifiable correlation squares in the spatial similarity matrix. Finding the boundary between these two squares defines another estimator for the optimal SVD threshold. Within a subspace, $|u_k|$ vectors are reshaped into 2D images and averaged to give an overview of the associated pixels (Fig. 4 b). As for the *in vivo* data (Fig. 10 a & e-Fig. 11 a,b,c), the tissue subspace is well represented by a small square of correlation. However, vectors in the *in vivo* blood subspace tend to be more correlated to their immediate neighbors than to the farthest vectors of the subspace. The *in vivo* blood correlation pattern has then a slightly elliptic shape, which can still be approximated by a square.

Interestingly, a square with weak correlation values appears as well in both experimental conditions and corresponds to the noise subspace. As it has mostly electronic and thermal origins, the noise part of the signal is considered to be Gaussian white noise, thus the associated spatial vectors are expected

to be uncorrelated as noise is spatially randomly spread. This gives rise to the possibility of double threshold SVD filter that would remove both tissue and noise signal. This will be discussed later in the paper.

E. Summary of All Estimators

All previously proposed estimators for automated singular value threshold are gathered in Table 1. The estimated threshold value is designated by the letter N.

III. MATERIALS AND METHODS

Both *in vitro* and *in vivo* experiments were performed with a programmable ultrafast ultrasound scanner (Aixplorer^{TM}, Supersonic Imagine, France) equipped with a SL10-2 ultrasonic probe (6.4MHz central frequency, 0.2mm pitch, 128 elements, 96% bandwidth and elevation focus at 35mm).

For the sake of clarity, methods and corresponding results have been matched with the following symbols:

- • *In-vitro*: assessment of estimators' performances
- ■ *In-vitro*: denoising with spatial similarity matrix
- ♦ *In-vivo*: applications of the spatial-similarity-based estimator

---

A. In Vitro Experiments: Assessment of Estimators' Performances •

1) Ultrasound Imaging Sequence •: Ultrafast ultrasound imaging was performed with tilted plane wave emission using 5 angles $[-6°, -3°, 0°, 3°, 6°]$ fired at a PRF of 5000Hz, in order to achieve a frame rate of 1000Hz after coherent compounding. This set of angles was repeated 600 times to build ultrafast cineloop of 600 frames. Ultrasonic pulses consisted in 3 cycles with central frequency 6.4 MHz fired with 40V peak-peak. All 192 elements of the probe were used for firing and only the 128 central elements were used for receive in order to avoid any side effect due to incomplete insonification by all the angles. RF data were acquired using a constant Time Gain Compensation (TGC) profile and an 80% FIR input filter bandwidth. In-phase/Quadrature image reconstruction was then performed from RF data using a simple delay and sum in-house beamformer with constant aperture $f/d = 1$.

2) Experimental Setup •: In order to quantitatively assess the relevance of all previously defined estimators, we developed an *in vitro* setup enabling calculation of the Contrast to Noise Ratio (CNR) based on the known geometrical position of the artificial vessel, which is far more reliable than doing quantification on *in vivo* experiments where the position of vessels is intrinsically unknown. We used a Doppler phantom (Model 523A, Cardiac Doppler Flow Phantom, ATS Laboratories, 404 Knowlton St., Bridgeport, CT 06608 USA), filled with blood-mimicking fluid (Model 707, Doppler Test Fluid, ATS Laboratories).The fluid circulation was insured by a variable-speed peristaltic tubing pump (Model 07528-10, Masterflex L/S, Cole-Parmer, USA). The canal had a diameter of 6mm and was imaged at a depth ranging from 35mm to 50mm approximately, with a tilting angle of 75° from
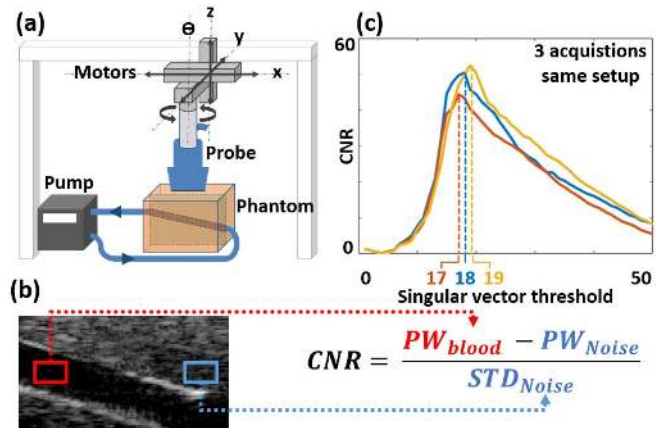

Fig. 5.   (a) Experimental setup (b) The CNR is computed using BMode image (c) For a given setup, the CNR curves are shown for 3 acquisitions (solid curves). The maximum of each curve gives access to the best singular vector threshold for the corresponding acquisition (dashed vertical lines).

the vertical axis. The SL10-2 ultrasonic probe was mounted on a motorized setup enabling three degrees of translation (Physik Instrumente (PI) translation stage VT-80, 0.8-μm one-directional repeatability, ± 10-μm bi-directional repeatability) and one degree of rotation (PI rotation stage DT-80, 0.01° one-directional repeatability, ± 0.2° bi-directional repeatability) as shown in Fig. 5(a). The goal was to reproduce different tissue motion conditions by moving the probe along (or around) different axes with several speeds. For each degree of freedom among the 4 possibilities, 6 flow speeds and 6 motor speeds were combined, boiling down to 144 different experimental conditions. Then, for a given triplet (k_{axis}, k_{flow}, k_{motion}) of motor axis, flow speed, and motor speed, 20 independent ultrasonic acquisitions were performed, which gives in the end a total 2880 acquisitions. Furthermore, in order to get closer to real-time imaging conditions, each acquisition was subdivided into frame ensembles of length $50, 100, 150$ and 200. For each ensemble length (EL), the 600-frame long acquisition was cut into 5 juxtaposed windows of size EL, with an overlap of 30 and 80 for those of size 150 and 200. The overall data structure[1] consequently contains 57600 different frame ensemble characterized by the indexes (k_{axis}, k_{flow}, k_{motion}, k_{acq}, k_{EL}, k_{win}) standing for 4 motor axes, 6 flow speed, 6 motor speed, 20 acquisition, 4 ensemble length, 5 windows. Although the different sub windows within the same acquisition may slightly overlap, we considered that for a given quadruplet (k_{axis}, k_{flow}, k_{motion}, k_{EL}), the 100 combinations of (k_{acq}, k_{win}) are independent measures. Finally, it means that we have 576 different experimental configurations (k_{axis}, k_{flow}, k_{motion}, k_{EL}), with 100 realizations for each one of them. Supplementary materials are available in the supplementary files /multimedia tab.

3) Evaluating Tissue/Blood Threshold Estimation Relevance •: In all cases, we were able to compute the CNR by segmenting the canal from the surrounding tissue on the B-Mode image. Two identical rectangles were delimited

---

[1]See Table in Supplementary Material I

TABLE I
10 PROPOSED ESTIMATORS FOR THE NUMBER OF SINGULAR VALUES REMOVED FROM THE SVD DECOMPOSITION

SVD FEATURE	ESTIMATOR NAME	DESCRIPTION	PARAM	PHYSICAL MEANING OR ASSUMPTION
SINGULAR VALUES Δ	Arbitrary threshold N_A	N is chosen as a fixed number of rejected singular values.	Yes	N_A is the size of the tissue subspace, and increases with the complexity of tissue motion
	Arbitrary threshold on the singular values magnitude N_S	N is chosen when $\frac{\lambda_N}{\sum_{k=1}^{Rank(S)} \lambda_k}$ reaches a given value in dB.	Yes	The partial contribution of a flow singular vector cannot exceed a certain proportion in the overall signal.
	Turning point of the singular value curve N_T	N is chosen when the singular value curve reaches a turning point (smallest curvature radius).	No	The singular values decrease follow different statistics if they describe tissue or blood flow.
	Energy of the blood signal N_E	N is set when $\frac{\sum_{k=N}^{Rank(S)} \lambda_k}{\sum_{k=1}^{Rank(S)} \lambda_k}$ reaches a given value in dB.	Yes	The ratio of blood energy and overall energy is always the same.
TEMPORAL SINGULAR VECTORS V	Central frequency N_{CF} – Half frequency band	N is set when the central frequency of the temporal singular vector V_k reaches a given value, on a half Fourier domain.	Yes	The tissue motion is restricted to a low speed range.
	Inflexion point of the central frequency N_{ACF} – Half frequency band	N is set to the first inflexion point of the central frequency curve.	No	Singular vector central frequency rapidly increases when moving from tissue subspace to blood subspace.
	Spectral standard deviation N_{STD} – Half frequency band	N is set when the second statistical moment of the temporal singular vector V_N spectrum reaches a given value.	Yes	Bandwidth of blood signal is higher than the one of tissue signal.
	Inflexion point of the spectral standard deviation N_{ASTD} – Half frequency band	N is set to the first inflexion point of the spectral standard deviation curve.	No	Singular vector bandwidth rapidly increases when moving from tissue subspace to blood subspace.
	99% Bandwidth inflexion point N_{BW}	N is set when the derivative of the 99% Bandwidth of the temporal singular vector V_k reaches a maximum.	No	The bandwidth of the temporal signal V_k shows a large increase when V_k changes from the description of tissue to the description of blood.
SPATIAL SINGULAR VECTORS U	Boundary between spatial subdomains N_{SS}	N is set at the boundary of the subdomains exhibited by the spatial similarity matrix $|U^*||U|$	No	Tissue and blood flow have different spatial extent, which is particularly relevant from an imaging point of view.

PARAM stands for "parametric".

at the same depth (37 to 40mm) in both canal and tissue (Fig. 5(b)). The mean Power Doppler is computed inside each area using Eq. 6.

$$PW(x, z) = \frac{1}{n_t} \sum_{t=1}^{n_t} \left| s^f(x, z, t) \right|^2 \quad (6)$$

Thus, the CNR is given by the difference of mean Power Doppler in each area divided by the Power Doppler standard deviation in the area outside the canal Fig. 5(b) [24]. It is conventionally used to quantify the ability to distinguish the structure of interest, the vasculature in present case, from the background. The main purpose of this *in vitro* setup is the following: for each window, we could test iteratively all the possible thresholds (N) within the range of the ensemble length to filter the signal and compute the resulting CNR on the filtered data at each step. The curve of the CNR as a function of N (Fig. 5 c) reaches a maximum when N is optimal. For each one of the 57600 ensembles previously described, this optimal N was found, and all estimators were also applied. We could quantify the relevance of each estimation by comparing the CNR obtained with the optimal N (i.e. the maximum CNR) and the CNR returned by the estimator N_X, X being $STD, f_c, \ldots$ It is important to highlight the fact that the relevance of an estimator is evaluated in terms of resulting CNR and not on its capacity to give a threshold as close as possible to the optimum. As a matter of fact, the steepness of the CNR curve around its maximum could differ from one experimental condition to another, hence, a shift of the

estimated N from its optimum could result in a severe drop of CNR or only a little decrease. The scope of this study being only the optimization of the SVD filter, we compare the CNR obtained with different threshold estimators against the maximum CNR achievable among all possible thresholds with SVD filtering. This maximum CNR will then be referred to as "optimal".

4) Parametric Estimators Optimization •*:* In Table 1, we introduced several parametric estimators, such as N_{CF} or N_{STD} : they both need a value for a Central Frequency or Frequency Standard Deviation cutoff. In routine imaging, these cutoffs should be chosen according to the application, but in the case of our phantom study we decided to conduct an exhaustive search of the best cutoff for every parametric estimator. We proceeded as follow: given a parametric estimator, for each cutoff within a wide range of values (e.g.: from 5Hz to 100Hz for the N_{CF} central frequency cutoff) the difference between the maximum possible CNR and the estimated CNR was averaged over the 57600 windows. The cutoff that returned the lowest mean CNR difference was chosen and used for all the study. This insures that all the parametric estimators were optimally tuned and gave the best of their possibilities.

5) Segmenting Subspaces on the Spatial Similarity Matrix •*:* In Fig. 4 we presented the possibility to visualize the tissue, blood and noise subspaces by considering the spatial similarity matrix $\mathbf{C}$ given by Eq. 5. As $\mathbf{C}$ is a symmetrical matrix,

TABLE II
ACOUSTIC PRESSURE, MECHANICAL INDEX (MI), THERMAL
INDEX (TI) AND ACOUSTIC POWERS (ISPPA AND ISPTA)
FOR IN VIVO EXPERIMENTS

	Peak Negative Pressure [MPa]	MI	TI	ISPTA [mW/cm²]	ISPPA [W/cm²]
Neonates	1.4	0.5	<1.02	190	62
Thyroid	1.4	0.5	<1.02	314	90
Carotid	1.4	0.5	<1.02	95	90
Kidney	1.4	0.5	<1.02	134	90

We refer to the Soft Tissue TI as both Cranial and Bone TI are not involved here. All sequences comply with the FDA Track 3 recommendations which are MI < 1.9, ISPTA < 720 mW/cm² and ISPPA < 190 W/cm².
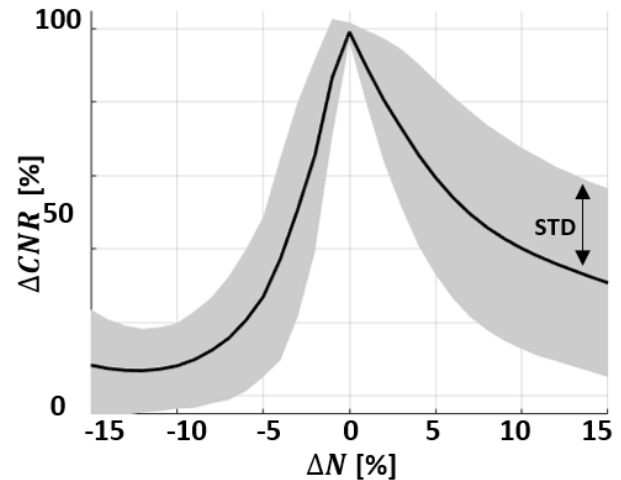
tissue and blood subspaces are typically represented by two juxtaposed symmetrical square areas followed by an area of weak correlation for the noise subspace. The boundaries of the subspaces were therefore obtained [2] by optimally fitting two juxtaposed squares to **C** using normalized correlation. Supplementary materials are available in the supplementary files /multimedia tab.

6) Noise Suppression ■: Subspaces segmentation on **C** allow the suppression of both tissue and noise signals. In order to assess the efficiency of the noise threshold estimator, we perform another exhaustive CNR analysis: for each of the 57600 windows, we optimally suppressed the tissue signal using the best tissue/blood threshold found in section III-A.3, then we iteratively tested every blood/noise threshold, recalculating the CNR at each step. The new maximum of this curve gives the optimal blood/noise threshold.

B. In vivo Experiments ♦

1) Neonate Brain ♦: Ultrafast Doppler sequences were acquired on the brains of healthy full-term neonates [25]. The previously introduced Aixplorer™ ultrasound scanner and SL10-2 probe were used. Two ultrasound sequences were designed, one with 2500 frames, compounded angles [−3°, 0°, 3°], PRF 9600Hz, Framerate 3200Hz, imaging depth [4mm – 50mm], used for big vessels imaging (Fig. 1, Fig. 2, and Fig. 3) and another one with 1600 frames, compounded angles [−5°, −3°, −1°, 1°, 3°], PRF 8000Hz, Framerate 1600Hz, imaging depth [2mm - 60mm] used for small vessels imaging (Fig. 10). These acquisitions were realized within a clinical research protocol (BELUGA) approved by the institutional review board (CCP: 'Comité de Protection des Personnes', i.e., Committee for the Protection of Persons, CCP agreement N° 120601) and local ethical committee. They strictly complies with the ethical principles for medical research involving human subjects of the World Medical Association Declaration of Helsinki, and with the FDA (Food and Drug Administration) recommendations (Track 3) detailed in Table 2. For each participant, written consent was obtained from parents.

2) Thyroid ♦: Ultrafast Doppler was also performed on the thyroid of an adult volunteer (Fig. 11 d). The sequence involved 600 frames, compounded angles [−5°, −4°, −3°,

---

[2]See Supplementary Material II for algorithm details

Fig. 6. Relative CNR deviation as a function of threshold under/overestimation.

$$\Delta N = \frac{N_{estim} - N_{max}}{EL} \qquad \Delta CNR = \frac{CNR_{estim} - CNR_{max}}{CNR_{max}}$$

N : Singular Value Threshold
EL : Ensemble Length
Estim : Obtained with a threshold estimator
Max : Obtained with the optimal threshold

−2°, −1°, 0°, 1°, 2°, 3°, 4°, 5°], PRF 15873Hz, Framerate 1443Hz, imaging depth [5mm - 25mm].

3) Carotid Plaque ♦: Atherosclerosis plaques in adult human carotid were imaged with Ultrafast Doppler (Fig. 11 e), using 1000 frames, compounded angles [−6°, −3.6°, −1.2°, 1.2°, 3.6°, 6°], PRF 4800Hz, Framerate 800Hz, imaging depth [2mm - 26mm]. The research has been validated by the local Ethical Committee ("Commission cantonale d'éthique de la recherche scientifique de Genève", standing for Geneva Cantonal Commission for the Ethics of Scientific Research) (Clinical Protocol R-15-253 - 2015-00045 of the 2015/10/30, modified the 2015/12/04) and strictly complies with the recommendations of the World Medical Association declaration of Helsinki.

4) Kidney ♦: Transplanted kidneys images (Fig. 11 f) were acquired on human adults using 1600 frames, compounded angles [−5°, −3°, −1°, 1°, 3°], PRF 8000Hz, Framerate 1600Hz, imaging depth [2mm - 60mm]. This clinical study was approved by the French national authorities (clinical trial number 2012-A01070-43).

IV. RESULTS

A. Small Errors on the Threshold Estimation Can Lead to Strong Drop in CNR ●

The overall study of the CNR curves obtained for the 57600 windows in the phantom dataset firstly revealed the importance of correctly estimating the tissue/blood threshold. Fig. 6 shows the consequences on the CNR of a wrong singular value threshold estimation. The relative error between the estimated threshold and the optimum has been normalized by the corresponding ensemble length in order to compare the

results on every windows regardless of their size. It appears that if the tissue subspace dimension is underestimated by 5% or more, the resulting CNR, namely $CNR_{estimated}$, will be below 40% of its maximum possible value, CNR_{max}. This is not surprising considering that a too low threshold produces the well-known flashing artefact. In the case of an overestimated threshold, the results are more variable from one ensemble to another, yet the trend is a clear decrease of the CNR as the relative thresholding error gets bigger, with an average CNR at 60% of its maximum for an error of +5%. These preliminary results shows that singular value thresholding truly is a matter of importance.

B. Comparing Estimators Overall Performances ●

The different estimators were evaluated on their capacity to provide a threshold that would result on a $CNR_{estimated}$ as close as possible to the maximum possible value for the considered window, CNR_{max}. For each window, the relative difference between CNR_{max} and $CNR_{estimated}$ was calculated. Therefore, it is possible to study the cumulative distribution function of this relative difference over the whole dataset. In other words, for a given relative difference between $CNR_{estimated}$ and CNR_{max}, one can look at how many estimations gave a result less than or equal to that value. A good estimator exhibits a curve as high as possible for low values of CNR errors. Moreover, the robustness is characterized by a rapidly increasing curve: hence, an estimator can have a lack of precision for low levels of CNR errors (typically <10%), but being robust enough for higher tolerated error (typically <30%). The optimal estimator reaches CNR_{max} in all cases, and therefore would exhibit on this graph a step curve reaching 100% starting from 0.

For this analysis, datasets are gathered as 100 trials of 576 different experimental configurations. The cumulative distribution function can then be computed for each trial. Finally the results are reported as a mean cumulative distribution function computed over the 576 setups, with surrounding area graphically delimiting the standard deviation obtained with the 100 trials. According to CNR error criterion, the estimator N_{SS} based on the spatial similarity matrix proved to be the more robust and efficient. In Fig. 7, we chose to represent this estimator's results against others. The estimators relying on half frequency band statistics such as N_{CF}, N_{STD}, N_{ACF} and N_{ASTD} were tested on both half bands.

Fig. 7 shows that the spatial similarity based estimator N_{SS} allows the determination of the threshold with good performances: in 72% of the acquisitions, $CNR_{estimated}$ is less than 10% below its maximum reachable value CNR_{max}. The second best candidate would be N_{STD} when computed on the negative frequency band. Interestingly, the choice of the band side for singular vector spectral statistics seems to have non negligible influence on the results. In the present case of the flow phantom, the flow moves toward the probe, which results (with a Z axis conventionally orientated away from the probe, *i.e.* downward in Fig. 5 a) in a negative frequency shift, and consequently of a dominance of the negative frequencies
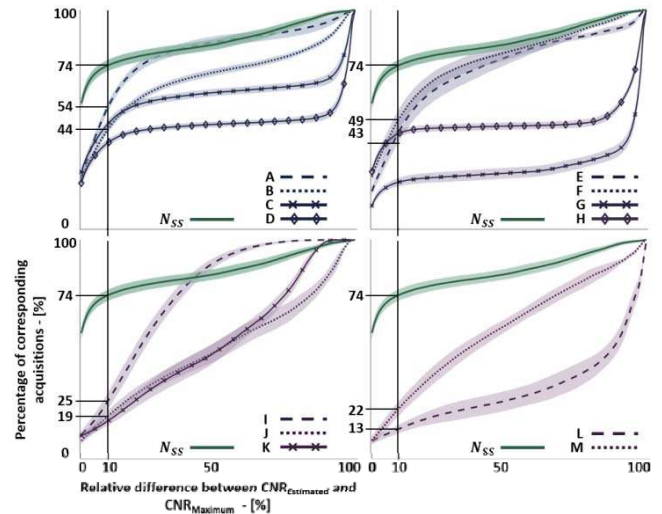
#	Estimator		Description	Feat.	Param
	N_{SS}		Spatial similarity matrix	U	No
A	N_{STD}	$f < 0$	Cutoff on the spectral STD	V	Yes
B	N_{STD}	$f > 0$	Cutoff on the spectral STD	V	Yes
C	N_{ASTD}	$f < 0$	Inflexion point of spectral STD	V	No
D	N_{ASTD}	$f > 0$	Inflexion point of spectral STD	V	No
E	N_{CF}	$f < 0$	Cutoff on central frequency	V	Yes
F	N_{CF}	$f > 0$	Cutoff on central frequency	V	Yes
G	N_{ACF}	$f < 0$	Inflexion point of central frequency	V	No
H	N_{ACF}	$f > 0$	Inflexion point of central frequency	V	No
I	N_E		Cutoff on the blood signal energy	Δ	Yes
J	N_T		Turning point of the singular value curve	Δ	No
K	N_S		Cutoff on singular value magnitude	Δ	Yes
L	N_{BW}		Inflexion point of the 99% bandwidth	V	No
M	N_A		Arbitrary threshold	Δ	Yes

Feat = SVD feature — Param = Parametric estimator

Fig. 7. Comparison of estimators' results. For different estimators, cumulative distribution function of ($CNR_{max} - CNR_{estimated}$) computed over the 576 setups with 100 independent measures. For each estimators, the 100 curves are averaged into one, surrounded by the ±STD area. Example : For the spatial similarity matrix estimator N_{SS}, in 74% of the estimations made among the 576 setups, the resulting CNR is only 10% (or less) below the maximum CNR.

in the singular vector spectrum. The estimator N_{CF} (for both bands $f > 0$ and $f < 0$) based on the central frequency of the temporal singular vectors is also quite efficient but less than N_{SS}, especially near the origin, which is the most important part of the graph. Furthermore, the adaptive estimators on Central Frequency and STD, N_{ACF} and N_{ASTD} proved to be less efficient than their optimized parametric version N_{CF} and N_{STD}. Besides, the whole frequency band was used for 99% bandwidth computation but the associated estimator N_{BW} showed very low performances. Regarding the singular value-based estimators, the arbitrary threshold on the number of singular values N_A, the arbitrary threshold on the magnitude of the singular values N_S, and the adaptive approach based on singular values radius of curvature N_T presents average performance, and turned out to be less precise and robust than the energetic estimator N_E relying on the singular values cumulative sum. As expected, it is more relevant to conjecture the energy of the whole blood subspace (estimator N_E) rather than assuming the relative energy of the first blood singular vector (estimator N_S), which has no physical meaning in itself. Finally, a fundamental conclusion that can be drawn from that figure is that among the 14 estimators presented, 10 exhibited better results than the arbitrary estimation. It justifies the

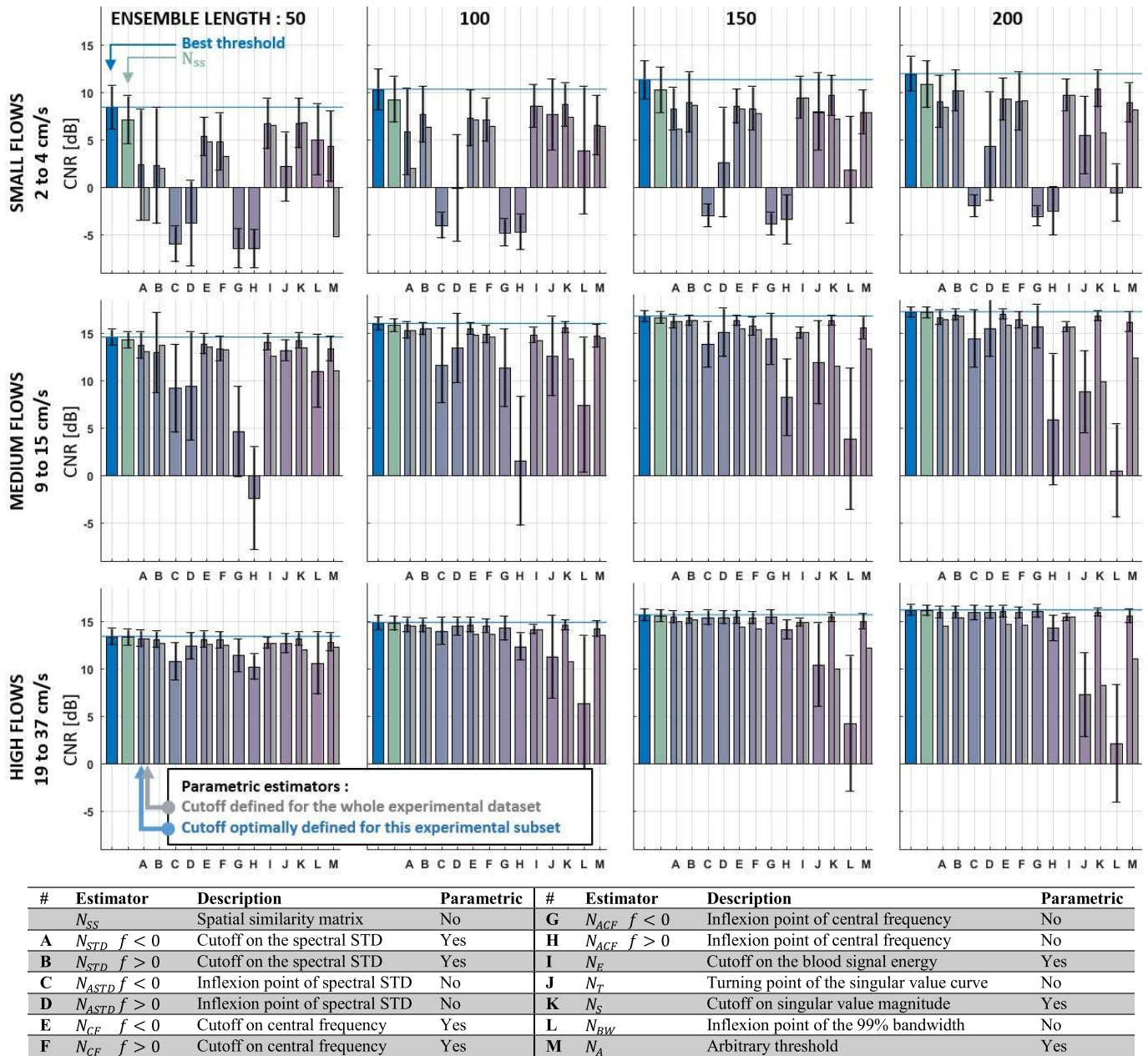| #	Estimator	Description	Parametric	#	Estimator	Description	Parametric
	N_{SS}	Spatial similarity matrix	No	G	$N_{ACF}\ f < 0$	Inflexion point of central frequency	No
A	$N_{STD}\ f < 0$	Cutoff on the spectral STD	Yes	H	$N_{ACF}\ f > 0$	Inflexion point of central frequency	No
B	$N_{STD}\ f > 0$	Cutoff on the spectral STD	Yes	I	N_E	Cutoff on the blood signal energy	Yes
C	$N_{ASTD} f < 0$	Inflexion point of spectral STD	No	J	N_T	Turning point of the singular value curve	No
D	$N_{ASTD} f > 0$	Inflexion point of spectral STD	No	K	N_S	Cutoff on singular value magnitude	Yes
E	$N_{CF}\ \ f < 0$	Cutoff on central frequency	Yes	L	N_{BW}	Inflexion point of the 99% bandwidth	No
F	$N_{CF}\ \ f > 0$	Cutoff on central frequency	Yes	M	N_A	Arbitrary threshold	Yes

Fig. 8. Estimators performances in different subsets of experimental conditions. The light blue bar and the blue line show the average best CNR reachable for each data subset. The green bar gives the average CNR obtained with the spatial similarity estimator N_{SS}. Parametric estimators are split in two half bars representing the two different cutoffs used: an optimized cutoff for the subset (left half bar) and a global cutoff (right half bar). The estimator order is the same as in Fig. 7.

purpose of this work and the necessity to improve singular value thresholding.

C. Influence of Ensemble Length and Flow Speed on Estimators Performances ●

Fig. 7 presents the estimators' performances in a general case where experimental conditions such as flow speed or clutter are not *a priori* known. But for some clinical applications, the blood speed can be expected to lie in a typical range. This knowledge as well as real-time processing requirements can put constraints on the ensemble length (EL). Therefore, in order to choose the most appropriate threshold estimator,

it could be useful to compare their performances in different subset of blood flows and EL. In order to challenge the estimators in strong clutter conditions, only the 3 highest tissue speeds were considered. This corresponds to probe motion speeds in the range [8-12] mm/s or [22-26] °/s. The 6 blood flow speeds available were clustered into 3 subgroups: small flows (2-4 cm/s), medium flows (9-15 cm/s), and high flows (19-37 cm/s). This 3 blood flow subgroups multiplied by the 4 EL lead to 12 data subsets. Finally, for a given subset (Flow, EL) and a given estimator, all CNR data are averaged among the corresponding experimental conditions. Then, the mean CNR is plotted in dB with its standard deviation, in Fig. 8.

Besides, section III-A.4 explained how the parametric estimators ($N_{CF}, N_{STD}, \ldots$) were tuned by finding the cutoff which minimizes the average between the maximum possible CNR and the estimated CNR. For each parametric estimator, we presents the results in two ways:

- with a cutoff optimized for the considered experimental subset (Flow, EL)
- with a cutoff optimized for the whole dataset (as used in Fig. 7)

These results are gathered in two adjacent half bars, the colored one on the left being computed with the cutoff optimized case-by-case, and the grey one on the right with the global cutoff.

This bar plot is very informative. We can highlight the following major points: first of all, small blood flows detection remains challenging for most estimators and benefits from long EL. Secondly, among all the non-parametric estimators (N_{SS} and bars C,D,G,H,J,L), the spatial similarity based estimators N_{SS} (green bar) seems to be the most robust across all data subsets, with an average CNR never less than 2dB under the maximum.

Lastly, parametric estimators such the arbitrary estimator N_A (bar M) with a finely tuned cutoff can have good performances if experimental conditions lie in a specific range of blood flow, with a fixed ensemble length. Their performances decrease if their cutoff is set for wider range of experimental conditions.

D. Removing Noise With a Double Threshold Approach ■

We previously introduced the possibility to identify both tissue and noise singular vector subspaces, using the spatial similarity matrix. Indeed, the CNR obtained with the best tissue/blood threshold can be further improved by optimally removing noise (Eq. 7). After defining a new maximum CNR for each window, the study of the CNR error distribution introduced in section 4.2 can be conducted again.

$$CNR_{max}^{(Tissue\ \&\ Noise\ suppression)} > CNR_{max}^{(Tissue\ suppression)}$$
(7)

Only two estimators are compared, both based on the spatial similarity matrix but one suppressing both tissue and noise (with two thresholds), and the other suppressing only tissue (with one threshold), the latter being precisely N_{SS} characterized as the best tissue/blood threshold estimators in section 4.2. Fig. 9 gathers the performances of these estimators. It is important to note that the green curve in IV-D and Fig. 9 describe the same estimator, but that the optimum CNR changed from one figure to another, implying a different shape. The first thing that comes out is that the definition of a new optimum CNR highly challenges the tissue/blood threshold only estimator performance: now for only 11% of the estimations, $CNR_{estimated}$ is 10% (or less) below $CNR_{max}^{(Tissue\ \&\ Noise\ suppression)}$. This highlights that tremendous CNR improvement can be achieve by suppressing tissue AND noise. Secondly, the adaptive double thresholds approach is quite efficient in that task (red curve).
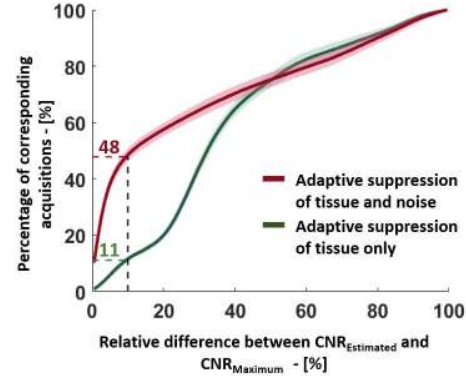

Fig. 9. Noise subspace determination and removal strongly increases the CNR.

E. In-vivo Experiments: Applications of the Spatial-Similarity-Based Estimator ♦

The spatial similarity matrix approach was applied to neonate brain imaging. Fig. 10 displays the Power Doppler images obtained for two different acquisitions with an arbitrary threshold (which was the starting point), an adaptive tissue/blood threshold or a double threshold on both tissue and noise. As already done in other studies [19], the arbitrary threshold was set to 60. For the first acquisition, the adaptively found value for the tissue/blood threshold was 50, which is close enough to the arbitrary value. The images obtained with these two threshold are comparable even though the adaptive method resulted in a better dynamic range. Conversely, the second acquisition suffer from a strong motion artifact when filtered with the arbitrary threshold, and only an adaptively determined value of 134 singular vectors to remove was able to suppress this artifact. This shows that even within the same clinical application, the optimal singular threshold may vary from one acquisition to another due to unpredictable movements. Moreover, for both acquisition, the spatial similarity matrix gave a blood/noise threshold around 640, and it clearly appeared that noise subspace removal can increase the dynamic range by several decibels. These improvements are estimated as follow. For the first acquisition in coronal view presented here (Fig. 10 a-d), a small vessel is segmented in the black dashed Region Of Interest (ROI) #1. Near the center of the image in ROI #2 is the brain's left ventricle. This structure is filled with hypo-echogenic fluid and can be taken as a reference for noise floor computation. Then, in addition to the CNR, the Signal To Noise (SNR) ratio is calculated for each image by dividing the average PW in ROI #1 by the average PW in ROI #2. For the arbitrary threshold, adaptive tissue and adaptive tissue+noise thresholds, the SNR is respectively 9.1dB, 10.5dB and 14.2dB. Similarly, the CNR values are 21.3dB, 22.7dB and 25.0 dB. The same analysis is conducted for the parasagittal acquisition. A vessel is segmented (ROI #3) alongside with a noisy area (ROI #4). For the images (f), (g) and (h), the resulting SNR are respectively 14.8dB, 23.0dB and 26.1dB; and the CNR 18.4dB, 33.7dB and 35.1dB. This shows the ability of the tissue and noise filter to improve the blood dynamic range.
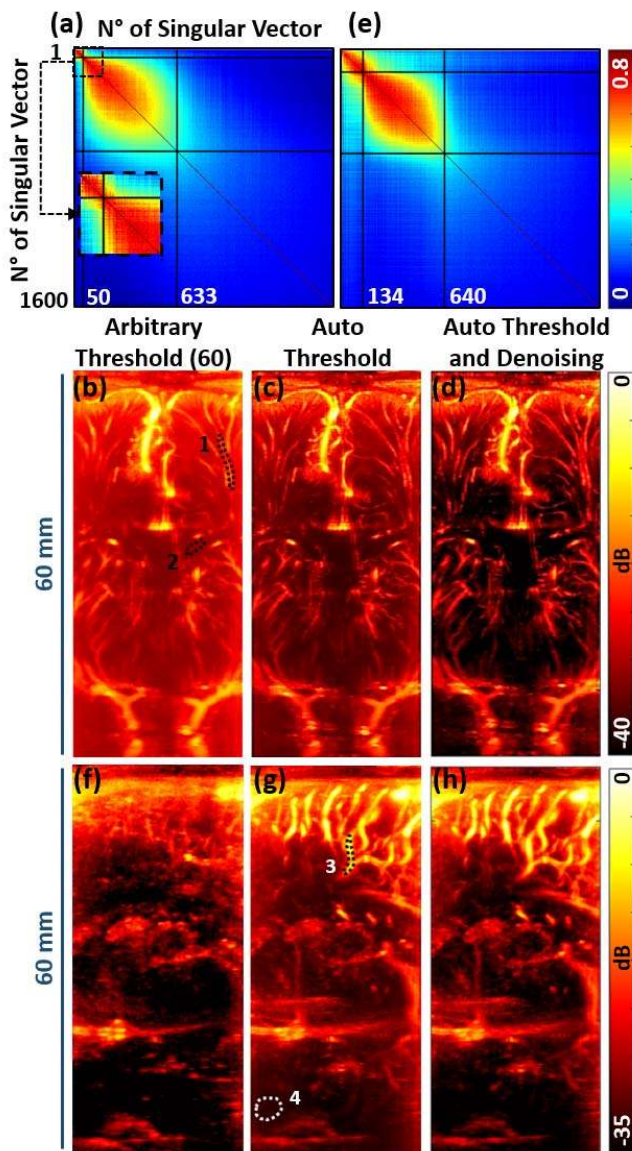
Fig. 10. In vivo assessments of thresholds relevance. Ultrafast Doppler acquisition on human neonate's brain in coronal (a-d) and parasagittal view (e-h), SVD-filtered with different thresholds. (a, e) Spatial similarity matrix of the two acquisitions, with a zoom on the 100 first indexes in the dashed box in (a). (b, f) The 60 first singular vectors were arbitrarily removed. (c, g) 50 and 134 singular vectors were respectively removed. These thresholds were adaptively computed using spatial similarity estimator. (d, h) The same feature was used to find the noise-subspace threshold, vectors from 633 to 1600 and 640 to 1600 were respectively removed. In (b), ROI #1 encompasses a small cortical penetrating vessel and ROI #2 the left ventricle. In (g), ROI #3 encompasses a small vessel and ROI #4 a noisy area.

The automated filter was tested in several experimental conditions, with several depths and flow ranges.[3] Fig. 11 shows the spatial similarity matrices and filtered Power Doppler images obtained for Ultrafast Doppler acquisitions on a human adult thyroid, carotid and transplanted kidney. It clearly appears that the singular value threshold vary from one clinical application to another, even in terms of relative proportion to the signal dimension. Supplementary materials are available in the supplementary files/multimedia tab.

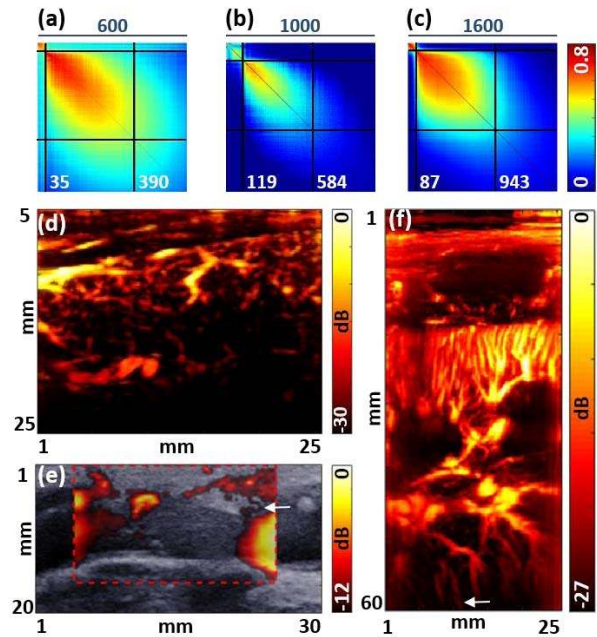[3]See Supplementary Movie and Sup. Mat. III for a real-time example

Fig. 11. In vivo application of adaptive thresholding. (a-c) Spatial similarity matrices with tissue/blood and blood/noise threshold (black lines). (d-f) Filtered Power Doppler images with both tissue and noise suppression. (a, d) Thyroid acquisition. (b, e) Carotid arteria with vascularised atherosclerosis plaque. Blood inside the lumen below the plaque is not detected due to plaque'fs wall calcification. A small vessel ($\varnothing$ 300μm) is detected within the plaque (white arrow). BMode is underplayed for better understanding. (c, f) Transplanted kidney. Vessel of diameter inferior to 1mm are still detected at a depth of 60mm (white arrow), allowing a clear visualisation of the renal cortex.

V. DISCUSSION

This paper tackles the problem of optimally selecting the blood signal subspace out of the SVD decomposition of an Ultrafast imaging ultrasonic acquisition. In this paper, we showed that a threshold N_{SS} based on the characteristics of the spatial singular vectors gave the best results, and even enabled to discriminate the blood signal subspace from two other subspaces, namely tissue and noise. Actually this result is not completely unexpected: the aim of the process being to obtain the best image possible, it feels natural to investigate what the left singular vectors u_k look like. This confirms that with Ultrafast ultrasound imaging strategies, space is at least as much important as time for clutter filtering, which was not the case with conventional focused ultrasound imaging relying on time-only clutter filter approaches.

The superiority of this threshold N_{SS} has been proven in a very controlled *in vitro* study with various flow speeds and tissue motion direction (in and out of plane) speeds totalizing 576 different experimental conditions. However we do not pretend that this can exhaustively reflect all the *in vivo* imaging condition. Homogenous echogenicity of the phantom and the presence of only one vessel cannot represent the variety of organs and vascular network encountered in general ultrasound imaging. That being said, it still enabled to quantitatively identify which estimator was the best in these conditions, a study that would have been doubtful with only *in vivo* datasets and manual segmentation of some vessels. The *in vivo* examples shown using this estimator confirmed that it

was indeed efficient, and other *in vivo* applications such as histotripsy monitoring led to parallel publication [23]

Considering the very diverse experimental conditions in our *in vitro* study, the strategy of choosing one single arbitrary value for the parametric estimators can be questioned, even if the best possible value was chosen for the complete set of experimental condition. However this fits in a clinical framework where a predefined filtering parameter needs to be tuned to match most situations, without a priori knowledge in terms of blood flow speeds and tissue motion.

Besides, it has been shown on Fig. 6 that even a small error on the threshold can sometimes have an important influence on the filter's efficiency. Therefore, the robustness of all presented estimators strongly relies on the quality of the involved statistics. Thus, it can be tricky to find the right turning point of the singular value distribution especially for long ensemble length. Similarly, identifying the tissue, blood and noise subspaces on the spatial similarity matrix is not always possible. Indeed, if in most of the case the tissue subspace is clearly revealed by a correlation square, the blood subspace can have a more elliptic shape as seen in Fig. 10 (a,e) and Fig. 11(a-c). The fact that blood spatial singular vectors are more correlated to their neighbors in the decomposition and not to whole subspace may be due to the variety of blood flow speeds (and consequently to the varying degree of correlation) in the field of view compared to the phantom study conditions.

Concerning the spatial similarity matrix, one has to keep in mind that its efficiency relies on the hypothesis that tissue and blood have different spatial distributions. This hypothesis is widely respected in most human organs applications and with frequencies below 10MHz as most of the time the detected vasculature does not cover the whole field of view. This assumption might be challenged in the case of higher frequencies such as superficial imaging or small animal imaging with high frequency probe (15MHz, resolution 100 μ m). As the field of view is narrower and as smaller vessels can be detected, the vascular tree may spread over an important part of the image, causing the spatial singular vector to be more correlated from one subspace to another.

A whole new field of application using Ultrafast ultrasound is functional imaging. Is that precise case, most studies described so far in the literature use the recording of Ultrafast Doppler images at different time points with the idea that the level of power Doppler in a pixel is proportional to the blood volume and that its time course reflects underlying neuronal activity. As such, it is really important that blood signal imaging remains quantitative and this new N_{SS} estimator for SVD clutter filter thresholding will need to be evaluated in that context. But we can reasonably expect this filter strategy to improve signal to noise ratio for functional imaging since it will be in the same time less sensitive to electronic noise and motion artefacts.

VI. Conclusion

This paper performed a quantitative assessment of several thresholding strategies for SVD based clutter filter. The temporal, energetic and spatial features of SVD were leveraged and compared in terms of resulting contrast-to-noise ratio. The correlation of spatial singular vectors magnitude was introduced, namely the spatial similarity matrix, and proved to be the most optimal and robust among all tested estimators. It enables the segmentation of both tissue and noise singular vectors subspaces. Its *in vivo* performance illustrated its ability to extract Doppler signal in very diverse conditions of tissue motion, blow flow characteristics, acquisitions length or imaging depth. The automation of SVD filtering highlights the high potential of Ultrafast Doppler for both diagnosis and functional imaging.

References

[1] M. Tanter and M. Fink, "Ultrafast imaging in biomedical ultrasound," *IEEE Trans. Ultrason., Ferroelect., Freq. Control*, vol. 61, no. 1, pp. 102–119, Jan. 2014.

[2] E. Mace, G. Montaldo, B. Osmanski, I. Cohen, M. Fink, and M. Tanter, "Functional ultrasound imaging of the brain: Theory and basic principles," *IEEE Trans. Ultrason., Ferroelect., Freq. Control*, vol. 60, no. 3, pp. 492–506, Mar. 2013.

[3] B. F. Osmanski, M. Pernot, G. Montaldo, A. Bel, E. Messas, and M. Tanter, "Ultrafast Doppler imaging of blood flow dynamics in the myocardium," *IEEE Trans. Med. Imag.*, vol. 31, no. 8, pp. 1661–1668, Aug. 2012.

[4] B. Y. Hur, J. Y. Lee, A. J. Chu, S. H. Kim, J. K. Han, and B. I. Choi, "UltraFast Doppler ultrasonography for hepatic vessels of liver recipients: Preliminary experiences," *Ultrasonography*, vol. 34, no. 1, pp. 58–65, Oct. 2015.

[5] E. Macé, G. Montaldo, I. Cohen, M. Baulac, M. Fink, and M. Tanter, "Functional ultrasound imaging of the brain," *Nature Methods*, vol. 8, no. 8, pp. 662–664, Aug. 2011.

[6] B. F. Osmanski, S. Pezet, A. Ricobaraza, Z. Lenkei, and M. Tanter, "Functional ultrasound imaging of intrinsic connectivity in the living rat brain with high spatiotemporal resolution," *Nature Commun.*, vol. 5, Oct. 2014, Art. no. 5023.

[7] L.-A. Sieu *et al.*, "EEG and functional ultrasound imaging in mobile rats," *Nature Methods*, vol. 12, no. 9, pp. 831–834, 2015.

[8] C. Demené *et al.*, "4D microvascular imaging based on ultrafast Doppler tomography," *Neuroimage*, vol. 127, pp. 472–483, Feb. 2015.

[9] B.-F. Osmanski, E. Lecarpentier, G. Montaldo, V. Tsatsaris, P. Chavatte-Palmer, and M. Tanter, "Discriminative imaging of maternal and fetal blood flow within the placenta using ultrafast ultrasound," *Sci. Rep.*, vol. 5, p. 13394, Sep. 2015.

[10] S. Bjaerum, H. Torp, and K. Kristoffersen, "Clutter filter design for ultrasound color flow imaging," *IEEE Trans. Ultrason., Ferroelect., Freq. Control*, vol. 49, no. 2, pp. 204–216, Feb. 2002.

[11] L. A. F. Ledoux, P. J. Brands, and A. P. G. Hoeks, "Reduction of the clutter component in Doppler ultrasound signals based on singular value decomposition: A simulation study," *Ultrason. Imag.*, vol. 19, no. 1, pp. 1–18, 1997.

[12] C. H. Alfred and L. Lovstakken, "Eigen-based clutter filter design for ultrasound color flow imaging: A review," *IEEE Trans. Ultrason., Ferroelect., Freq. Control*, vol. 57, no. 5, pp. 1096–1111, May 2010.

[13] S. Bjaerum, H. Torp, and K. Kristoffersen, "Clutter filters adapted to tissue motion in ultrasound color flow imaging," *IEEE Trans. Ultrason., Ferroelect., Freq. Control*, vol. 49, no. 6, pp. 693–704, Jun. 2002.

[14] L. Lovstakken, S. Bjaerum, K. Kristoffersen, R. Haaverstad, and H. Torp, "Real-time adaptive clutter rejection filtering in color flow imaging using power method iterations," *IEEE Trans. Ultrason., Ferroelect., Freq. Control*, vol. 53, no. 9, pp. 1597–1608, Sep. 2006.

[15] D. E. Kruse and K. W. Ferrara, "A new high resolution color flow system using an eigendecomposition-based adaptive filter for clutter rejection," *IEEE Trans. Ultrason., Ferroelect., Freq. Control*, vol. 49, no. 10, pp. 1384–1399, Oct. 2002.

[16] E. J. Candès, C. A. Sing-Long, and J. D. Trzasko, "Unbiased risk estimates for singular value thresholding and spectral estimators," *IEEE Trans. Signal Process.*, vol. 61, no. 19, pp. 4643–4657, Oct. 2012.

[17] E. J. Candès, X. Li, Y. Ma, and J. Wright, "Robust principal component analysis?" *J. ACM*, vol. 58, no. 1, pp. 1–37, 2009.

[18] R. Otazo, E. J. Candès, and D. K. Sodickson, "Low-rank plus sparse matrix decomposition for accelerated dynamic MRI with separation of background and dynamic components," *Magn. Reson. Med.*, vol. 73, no. 3, pp. 1125–1136, 2014.

[19] C. Demené *et al.*, "Spatiotemporal clutter filtering of ultrafast ultrasound data highly increases Doppler and fUltrasound sensitivity," *IEEE Trans. Med. Imag.*, vol. 34, no. 11, pp. 2271–2285, Nov. 2015.

[20] V. A. Marčenko and L. A. Pastur, "Distribution of eigenvalues for some sets of random matrices," *Math. USSR-Sbornik*, vol. 1, no. 4, pp. 457–483, 1967.

[21] W. F. Walker and G. E. Trahey, "A fundamental limit on the performance of correlation-based phase correction and flow estimation techniques," *IEEE Trans. Ultrason., Ferroelect., Freq. Control*, vol. 41, no. 5, pp. 644–654, Sep. 1994.

[22] S. Hovda, H. Rue, and B. Olstad, "New echocardiographic imaging method based on the bandwidth of the ultrasound Doppler signal with applications in blood/tissue segmentation in the left ventricle," *Comput. Methods Programs Biomed.*, vol. 92, no. 3, pp. 279–288, 2008.

[23] B. Arnal, J. Baranger, C. Demené, M. Tanter, and M. Pernot, "*In vivo* real-time cavitation imaging in moving organs," *Phys. Med. Biol.*, vol. 62, no. 3, pp. 843–857, Feb. 2017.

[24] F. W. Mauldin, D. Lin, and J. A. Hossack, "The singular value filter: A general filter design strategy for PCA-based signal separation in medical ultrasound imaging," *IEEE Trans. Med. Imag.*, vol. 30, no. 11, pp. 1951–1954, Nov. 2011.

[25] C. Demené *et al.*, "Ultrafast Doppler reveals the mapping of cerebral vascular resistivity in neonates," *J. Cerebral Blood Flow Metabolism*, vol. 34, no. 6, pp. 1009–1017, 2014.

[26] E. Tiran *et al.*, "Transcranial functional ultrasound imaging in freely moving awake mice and anesthetized young rats without contrast agent," *Ultrasound Med. Biol.*, vol. 43, no. 8, pp. 1679–1689, 2017.